Supporting Information

Synthesis Mechanism and Luminescence Mechanism of 1D Organic Metal Halides with Mixed Single-stranded and Double-stranded chains

Jiajing Zhou,† Dongjie Tian,§ Kunjie Song, † Litipu Aihaiti, †Wenhao Bai, † Rundong Tian, † and Rong-Jun Xie*, †

† Fujian Province Key Laboratory of Surface and Interface Engineering for High-Performance Materials, and College of Materials, Xiamen University, 361005 Xiamen, China

§ College of Chemistry and Chemical Engineering, Xiamen University, 361005 Xiamen, China

EXPERIMENTAL METHODS

Materials. All experiments were carried out in the air atmosphere with standard Schlenk technology. $PbBr_2$ was purchased from Acme (Zhengzhou) Chemical Industry Company. Adenine and HBr (47 wt% in water) were purchased from Meryer (Shanghai) Chemical Technology Company. Acetone were purchased from Sinopharm Chemical Reagent Company and stored in accordance with standard procedures.

Synthesis of 1. Adenine (0.135 g, 1 mmol) and $PbBr_2$ (1.101 g, 3 mmol) were mixed in 10 mL HBr (47%, in H_2O) and heated to reflux (the reactants dissolve completely). The reaction system was cooled slowly. After 24 h, white rod-like crystals were formed. Then the crystals were washed with cold acetone, and bulk crystals of **1** were obtained.

Synthesis of 2. Adenine (0.135 g, 1 mmol) and $PbBr_2$ (1.835 g, 5 mmol) were mixed in 13 mL of 47% HBr (in H_2O) and heated to reflux, resulting in complete dissolution of the reactants. The reaction mixture was then cooled gradually. After 24 hours, white rod-like crystals formed. These crystals were washed with cold acetone, yielding bulk crystals of compound **2**.

Physical Measurements.

Single-crystal X-ray diffraction (SCXRD) data were conducted on an Synergy Diffraction Microfocus spot diffractometer with graphite-monochromatized Cu Kα radiation (λ = 1.54178 Å) at 100K, operating at 50 kV and 1 mA under N_2 flow. The multiscan absorption corrections were applied using the program CrysAlis. The crystal structure was solved and refined by least squares on F2 using SHELXTL and OLEX2 programs. The powder X-ray diffraction (PXRD) analysis was performed using a Bruker, D8 ADVANCE X-ray powder diffractometer with Cu Kα (λ = 1.5406 Å) operating at 40 kV/40 mA. Optical images were obtained by widefield microscopes (Leica LAS X). Fourier transform infrared (FT-IR) spectra were recorded from 500 to 4000 cm^{-1} using a Thermo Scientific Nicolet iS10 FT-IR spectrometer (Waltham). Element content (Pb and Br) were determined on an inductively coupled-source mass spectrometer (ICP-MS, Icap Qc, Thermo Fisher Scientific). TGA was recorded from 20℃ to 800℃ with the 5℃ min^{-1} in nitrogen atmosphere on a TA Instruments SDT Q600 in a N_2 atmosphere.

Optical Measurements.

Optical diffuse reflectance measurements were performed using a CACY5000 UV−vis NIR spectrometer operating in the 200−800 nm region at room temperature and $BaSO_4$ as the 100% reflectance reference. The reflectance data were converted to absorption according to the Kubelka−Munk equation: $\alpha/S = (1 - R)^2 (2R)^{-1}$, where R is the reflectance, α and S are the absorption and scattering coefficients, respectively. Steady-state photoluminescence spectra were obtained on an Edinburgh Instruments FLS1000 spectrophotometer at room temperature. Time-resolved photoluminescence (TRPL) spectra were acquired using Edinburgh FLS1000 spectrophotometer equipped with a xenon lamp and a TCSPC module (diode laser excitation at λ = 375 nm). The PLQY was determined using an Edinburgh FLS1000 spectrophotometer with an integrating sphere. Temperature-dependent emission and decay data were collected using the FLS1000 spectrophotometer equipped with a closed-cycle cryostat (DE202, Advanced Research Systems) at a series of temperature from 78 to 300 K.

Calculations.

In this study, we utilized first-principles calculations[1-2] to conduct density functional theory (DFT)

calculations employing the generalized gradient approximation (GGA) according to the Perdew-Burke-Ernzerhof (PBE) formulation.[3] Projected augmented wave (PAW) potentials[4-5] were selected to describe the ionic cores, incorporating valence electrons with a plane wave basis set possessing a kinetic energy cutoff of 450 eV. The Gaussian smearing method was applied to permit partial occupancies of the Kohn−Sham orbitals, with a width of 0.05 eV. Self-consistency of the electronic energy was achieved when the energy change fell below 10^{-5} eV. Geometric optimization was considered convergent when the energy change was smaller than 0.02 eV $Å^{-1}$. The structural optimization encompassed both atomic coordinate relaxation and lattice parameter optimization. The weak interaction was described by DFT+D3 method using empirical correction in Grimme's scheme[6-7]. For the optimization of both geometry and lattice size, the BrHouin zone integration was performed with a Monkhorst-pack k-point mesh of 4*3*1. For the excited state optimization, the same computational settings were employed in conjunction with time-dependent density functional theory (TDDFT),[8] a method well-suited for exploring electronic excitations. This dual-level approach provides a comprehensive understanding of both ground and excited state properties.

Table S1. Crystal data and structure refinement for **1**.

Sample	**1**
Empirical formula	$C_{10}H_{16}Br_7N_{10}OPb_{1.5}$
Formula weight	1162.48
Temperature/K	100
Crystal system	triclinic
Space group	$P\bar{1}$
a (Å)	6.0058(2)
b (Å)	10.2154(2)
c (Å)	21.6311(5)
α (°)	85.801 (2)
β (°)	85.807 (2)
γ (°)	75.400 (2)
Volume/Å^3	1278.75(6)
Z	2
ρ_{calc} g/cm^3	3.019
μ/mm^{-1}	32.101
F(000)	1044.0
Radiation	Cu Kα(λ=1.54184)
2θ range for data collection/°	8.21 to 150.356
Index ranges	-7≤ h ≤7, -12≤ k ≤11, -26≤ l ≤26,
Reflections collected	14040
Independent reflections	4990[R_{int}=0.0488, R_{sigma}=0.0413]
Data/restraints/parameters	4990/0/274
Goodness-of-fit on F^2	1.071
Final R indexes [I>=2σ(I)]	R_1=0.0441, ωR_2=0.1206
Final R indexes [all data]	R_1=0.0455, ωR_2=0.1222
Largest diff. peak/hole/e Å^{-3}	4.62/-1.64

Table S2. Elemental analysis (by ICP-MS) of Pb and Br.

Element	Pb	Br
Mass concentration (μg/L)	43.619	118.321
Molar mass (g/mol)	207.20	79.90
Molar concentration (mmol/L)	0.2105	1.4808
Relative molar ratio	2.00	14.06

The ICP-MS measurement was used to determine the relative atom ratios of Pb and Br. The result shows that the element ratio of Pb/Br is 2/14.06, which was highly close to the theoretical value 2/14.

Table S3. Experimental bond lengths and angles of the $[PbBr_5]^{3-}$ groups of single-stranded chain in **1**.

Bonds	Length (Å)	Angles	Degrees (°)
Pb1–Br1$^{\#1}$	3.00290(9)	Br1–Pb1–Br1$^{\#1}$	180.0
Pb1–Br1	3.00290(11)	Br1–Pb1–Br4	85.413(15)
Pb1–Br4$^{\#2}$	3.0225(7)	Br1–Pb1–Br4	94.587(15)
Pb1–Br4	3.0225(7)	Br1–Pb1–Br4$^{\#2}$	85.414(15)
Pb1–Br8$^{\#2}$	2.9873(9)	Br1$^{\#1}$–Pb1–Br4	94.586(15)
Pb1–Br8	2.9873(9)	Br4–Pb1–Br4$^{\#2}$	180.0
		Br8–Pb1–Br1	85.453(19)
		Br8$^{\#2}$–Pb1–Br1	85.453(19)
		Br8–Pb1–Br1	94.547(19)
		Br8–Pb1–Br1$^{\#1}$	94.547(19)
		Br8–Pb1–Br4	90.65(2)
		Br8$^{\#2}$–Pb1–Br4	89.35(2)
		Br8–Pb1–Br4	90.65(2)
		Br8–Pb1–Br4$^{\#2}$	89.35(2)
		Br8–Pb1–Br8$^{\#2}$	180.0

Table S4. Experimental bond lengths and angles of the $[Pb_2Br_9]^{5-}$ groups of double-stranded chain in **1**.

Bonds	Length (Å)	Angles	Degrees (°)
Pb2–Br2	3.0302(8)	Br2–Pb2–Br3	89.26(2)
Pb2–Br3$^{\#1}$	3.0964(8)	Br2–Pb2–Br6	95.745(15)
Pb2–Br3	2.9238(8)	Br3$^{\#1}$–Pb2–Br2	92.39(2)
Pb2–Br5	2.9263(8)	Br3–Pb2–Br3	172.07(3)
Pb2–Br6	3.0660(3)	Br3$^{\#1}$–Pb2–Br5	94.92(2)
Pb2–Br7	2.9369(8)	Br3–Pb2–Br6	90.323(18)
		Br3$^{\#1}$–Pb2–Br7	83.51(3)
		Br5–Pb2–Br2	172.55(2)
		Br5–Pb2–Br3	83.69(2)
		Br5–Pb2–Br6	85.649(17)
		Br5–Pb2–Br7	86.97(2)
		Br6–Pb2–Br3	81.795(17)
		Br7–Pb2–Br2	92.45(2)
		Br7–Pb2–Br3	104.18(2)
		Br7–Pb2–Br6	169.94(2)

Table S5. Changes of bond lengths between ground state and excited state of the $[PbBr_5]^{3-}$ groups of single-stranded chain in **1**.

	Pb1–Br1$^{\#1}$	Pb1–Br1	Pb1–Br4$^{\#2}$	Pb1–Br4	Pb1–Br8$^{\#2}$	Pb1–Br8
Ground state	3.003	3.003	3.023	3.023	2.987	2.987
Excited state	3.031	3.005	3.015	2.967	3.528	2.767

Table S6. Changes of bond angles between ground state and excited state of the $[PbBr_5]^{3-}$ groups of single-stranded chain in **1**.

	Br1–Pb1–Br4	Br1–Pb1–Br4$^{\#2}$	Br1$^{\#1}$–Pb1–Br4	Br1$^{\#1}$–Pb1-Br4$^{\#2}$	Br8–Pb1–Br1	Br8$^{\#2}$–Pb1–Br1
Ground state	85.413	94.587	85.413	94.587	85.453	85.453
Excited state	82.500	83.028	95.483	98.197	84.336	82.979
	Br8–Pb1–Br1$^{\#1}$	Br8$^{\#2}$–Pb1–Br1$^{\#1}$	Br8–Pb1–Br4	Br8–Pb1–Br4$^{\#2}$	Br8$^{\#2}$–Pb1–Br4	Br8$^{\#2}$–Pb1–Br4$^{\#2}$
Ground state	94.547	94.547	90.653	89.356	90.653	89.356
Excited state	91.066	98.468	95.716	80.970	95.812	89.514

Table S7. Changes of bond lengths between ground state and excited state of the $[Pb_2Br_9]^{5-}$ groups of double-stranded chain in **1**.

	Pb2–Br2	Pb2–Br3$^{\#1}$	Pb2–Br3	Pb2–Br5	Pb2–Br6	Pb2–Br7
Ground state	3.030	3.096	2.924	2.926	3.066	2.937
Excited state	3.029	3.056	2.944	3.002	2.882	2.945
	Pb2–Br2	Pb2–Br3$^{\#1}$	Pb2–Br3	Pb2–Br5	Pb2–Br6	Pb2–Br7
Ground state	3.030	3.096	2.924	2.926	3.066	2.937
Excited state	3.004	2.951	3.055	2.987	3.259	3.385

Table S8. Changes of bond angles between ground state and excited state of the $[Pb_2Br_9]^{5-}$ groups of double-stranded chain in **1**.

	Br2–Pb2–Br3	Br2–Pb2–Br6	Br3–Pb2–Br2	Br3–Pb2–Br5	Br3–Pb2–Br6	Br3–Pb2–Br7
Ground state	89.263	95.745	92.394	94.926	90.323	83.515
Excited state	95.301	88.248	84.726	86.091	95.380	91.407
	Br5–Pb2–Br3	Br5–Pb2–Br6	Br5–Pb2–Br7	Br6–Pb2–Br3	Br7–Pb2–Br2	Br7–Pb2–Br3
Ground state	83.690	85.649	86.974	81.795	92.453	104.186
Excited state	90.907	88.993	94.082	86.960	102.353	76.611
	Br2–Pb2–Br3	Br2–Pb2–Br6	Br3–Pb2–Br2	Br3–Pb2–Br5	Br3–Pb2–Br6	Br3–Pb2–Br7
Ground state	89.263	95.745	92.394	94.926	90.323	83.515
Excited state	88.979	83.039	92.880	92.126	87.265	99.880
	Br5–Pb2–Br3	Br5–Pb2–Br6	Br5–Pb2–Br7	Br6–Pb2–Br3	Br7–Pb2–Br2	Br7–Pb2–Br3
Ground state	83.690	85.649	86.974	81.795	92.453	104.186
Excited state	94.501	81.522	82.190	103.438	82.503	91.400

Table S9. Crystal data and structure refinement for **2**.

Sample	**2**
Empirical formula	$C_{10}H_{18}Br_8N_{10}O_2Pb_2$
Formula weight	1364.00
Temperature/K	150
Crystal system	monoclinic
Space group	$P2_1/c$
a (Å)	6.0771(2)
b (Å)	18.3935(7)
c (Å)	25.4976(9)
α (°)	90
β (°)	94.3470 (10)
γ (°)	90
Volume/Å^3	2841.90.(17)
Z	4
ρ_{calc} g/cm^3	3.188
μ/mm^{-1}	23.109
F(000)	2432.0
Radiation	Mo Kα(λ=0.71073)
2θ range for data collection/°	4.428 to 52.826
Index ranges	-7≤ h ≤7, -23≤ k ≤23, -31≤ l ≤31,
Reflections collected	51113
Independent reflections	5842[R_{int}=0.0881, R_{sigma}=0.0482]
Data/restraints/parameters	5842/0/295
Goodness-of-fit on F^2	0.998
Final R indexes [I>=2σ(I)]	R_1=0.0314, ωR_2=0.0584
Final R indexes [all data]	R_1=0.0621, ωR_2=0.0668
Largest diff. peak/hole/e Å^{-3}	0.87/-0.88

Table S10. Experimental bond lengths and angles of the $[PbBr_4]^{2-}$ groups of **2**.

Bonds	Length (Å)	Angles	Degrees (°)
Pb1–Br5	2.9312(9)	Br5–Pb1–Br6	173.11(2)
Pb1–Br6	3.1020(9)	Br5–Pb1–Br7	89.70(3)
Pb1–Br7	2.9635(9)	Br5–Pb1–Br8	82.40(2)
Pb1–Br8[1]	3.0660(8)	Br5–Pb1–Br8[1]	94.06(2)
Pb1–Br8	3.0154(8)	Br5–Pb1–Br9	90.47(2)
Pb1–Br9	3.0398(9)	Br7–Pb1–Br6	86.18(2)
Pb2–Br3	2.8336(8)	Br7–Pb1–Br8[1]	89.69(2)
Pb2–Br4	2.8828(9)	Br7–Pb1–Br8	92.73(2)
Pb2–Br6	3.1816(9)	Br7–Pb1–Br9	177.16(2)
Pb2–Br9	3.1809(9)	Br8–Pb1–Br6	92.29(2)
Pb2–Br10	3.0147(8)	Br8[1]–Pb1–Br6	91.43(2)
Pb2–Br10[1]	3.0666(8)	Br8–Pb1–Br8[1]	175.69(3)
		Br8–Pb1–Br9	90.10(2)
		Br9–Pb1–Br6	93.92(2)
		Br9–Pb1–Br8[1]	87.47(2)
		Br3–Pb2–Br4	88.05(2)
		Br3–Pb2–Br6	172.27(2)
		Br3–Pb2–Br9	95.49(2)
		Br3–Pb2–Br10[1]	86.59(2)
		Br3–Pb2–Br10	97.52(2)
		Br4–Pb2–Br6	86.51(2)
		Br4–Pb2–Br9	175.85(2)
		Br4–Pb2–Br10[1]	89.78(2)
		Br4–Pb2–Br10	91.44(2)
		Br9–Pb2–Br6	89.75(2)
		Br10[1]–Pb2–Br6	87.91(2)
		Br10–Pb2–Br6	88.11(2)
		Br10[1]–Pb2–Br9	88.29(2)
		Br10–Pb2–Br9	90.24(2)
		Br10–Pb2–Br10[1]	175.75(4)

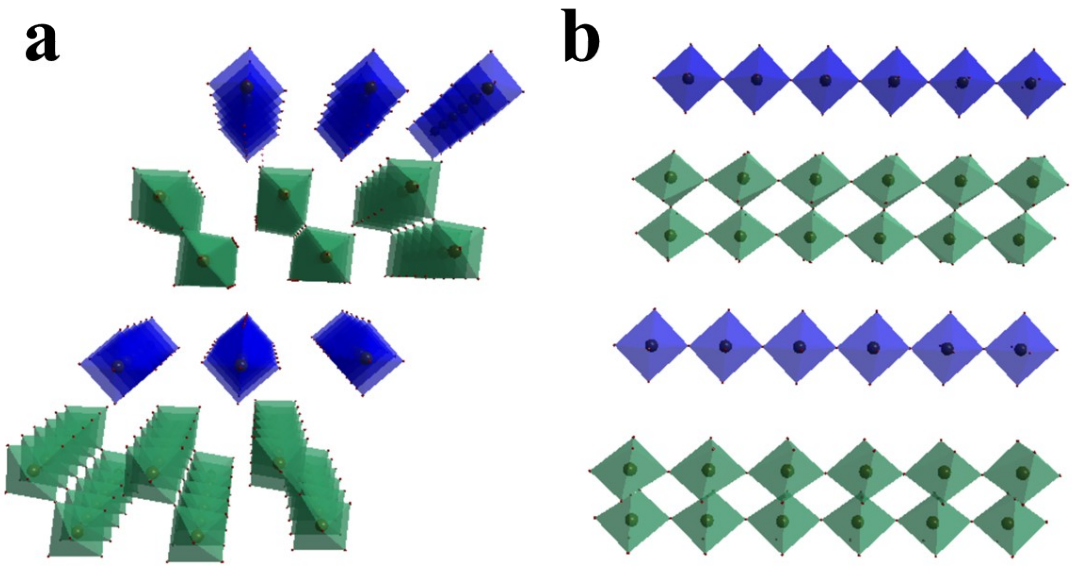

Figure S1. a), b) Detailed view of the crystal structure **1**.

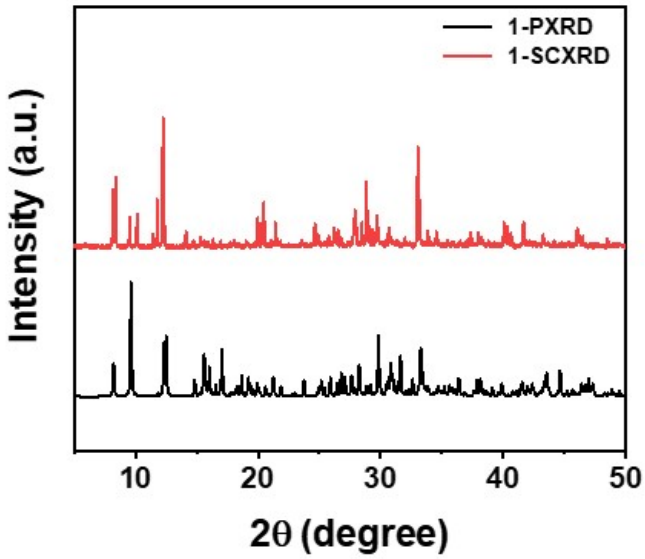

Figure S2. PXRD patterns and the simulated XRD patterns based on the single crystal of **1**.

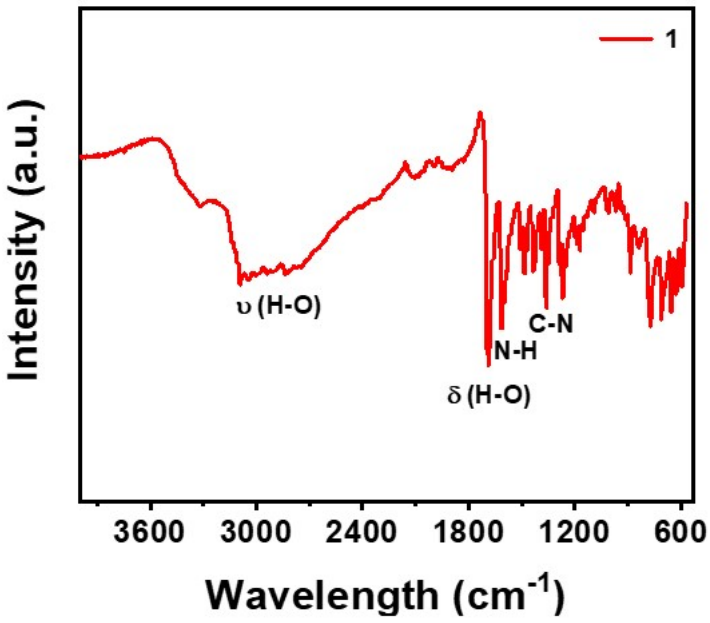

Figure S3. FTIR spectrum of **1** crystal.

The broad absorption in the range of 3000-3600 cm^{-1} is assigned to H-O stretching vibration ($\upsilon_{H\text{-}O}$) of the combined water, and the narrow absorption from 1600 to 1700 cm^{-1} is assigned to H-O bending vibration ($\delta_{H\text{-}O}$) of the combined water. The absorption peaks centered at 1609 cm^{-1} is assigned to N-H bending vibration. The absorption peaks centered at 1357 cm^{-1} is assigned to C-N stretching vibration. The result verifies the existence of the organic cations and coordinating water in 1D-OMH **1**.

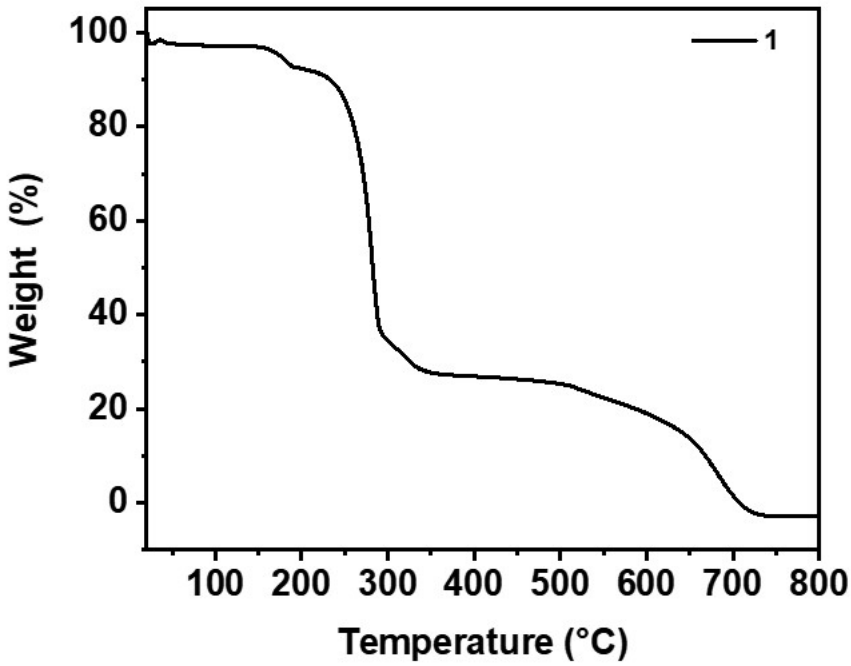

Figure S4. The TG curve of **1**.

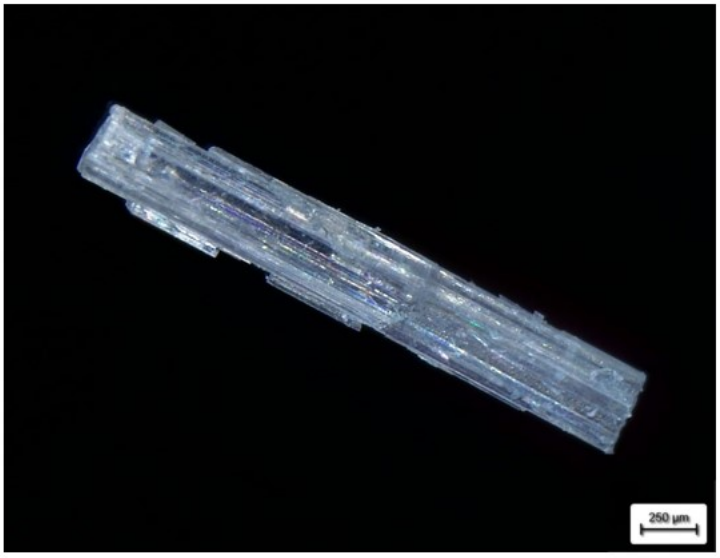

Figure S5. Images of **1** single crystals.

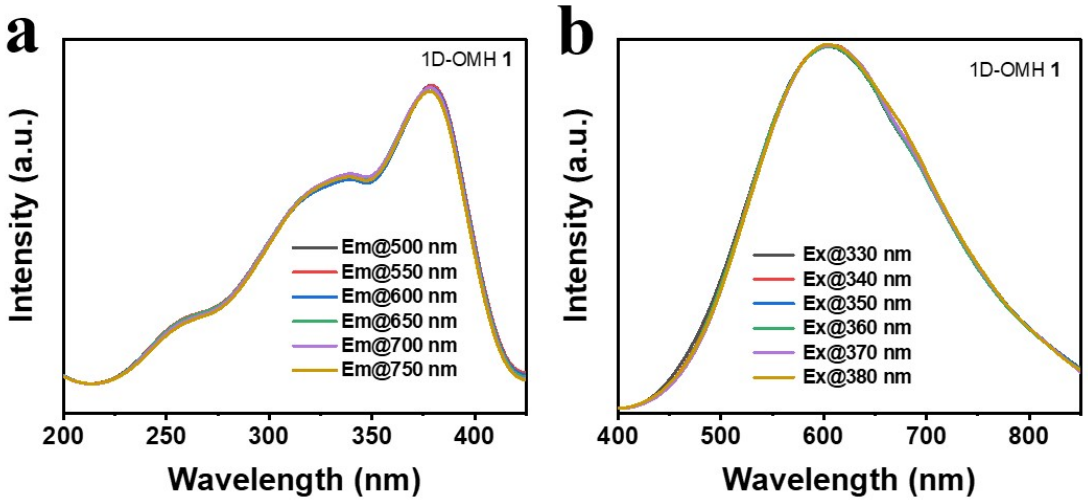

Figure S6. a) The PLE spectra of 1D-OMH **1** monitoring at 500 nm, 550 nm, 600 nm, 650 nm 700 nm and 750 nm, respectively. b) The excitation wavelength-dependent PL spectra of 1D-OMH **1**. (the excitation wavelength ranged from 330 nm to 380 nm and the interval is 10 nm.

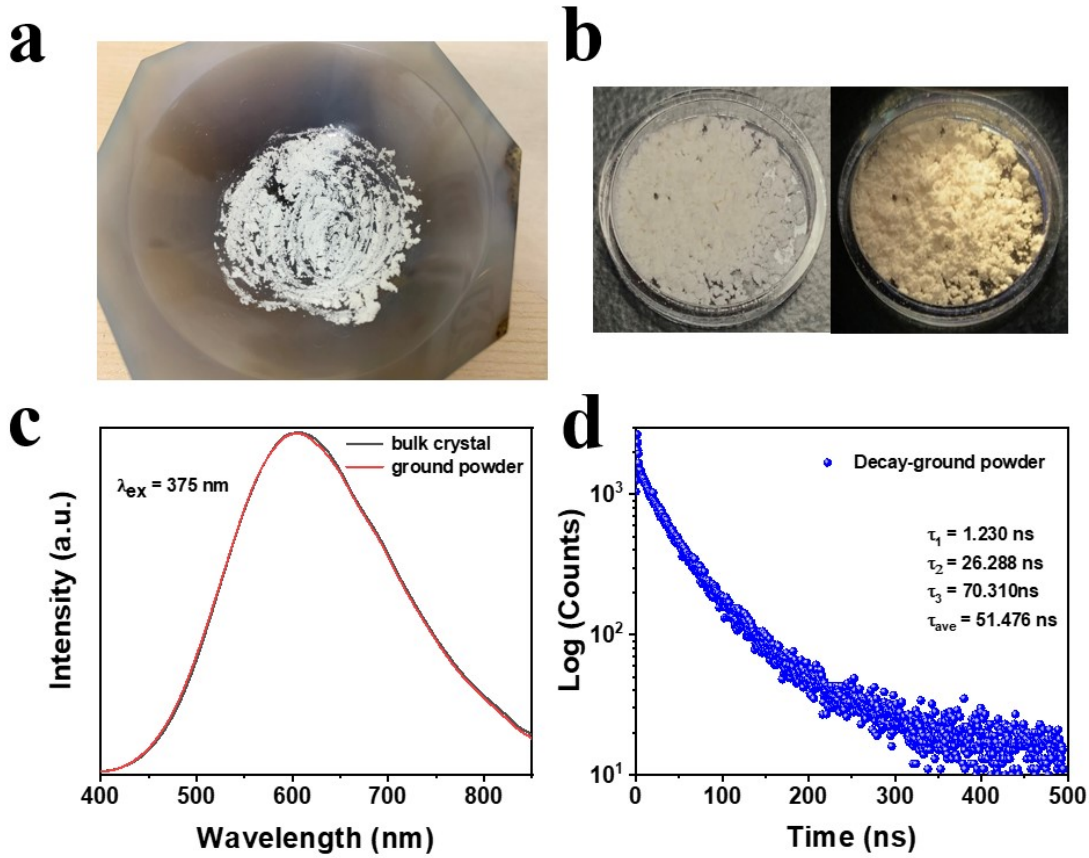

Figure S7. a) Grinding single crystals into powder using a mortar and pestle. b) Images under natural light and 365 nm UV light excitation of ground powders of 1D-OMH **1**. c) The PL spectra of bulk crystals and ground powders of 1D-OMH **1**. d) The time-resolved decay curves of ground powders of 1D-OMH **1**.

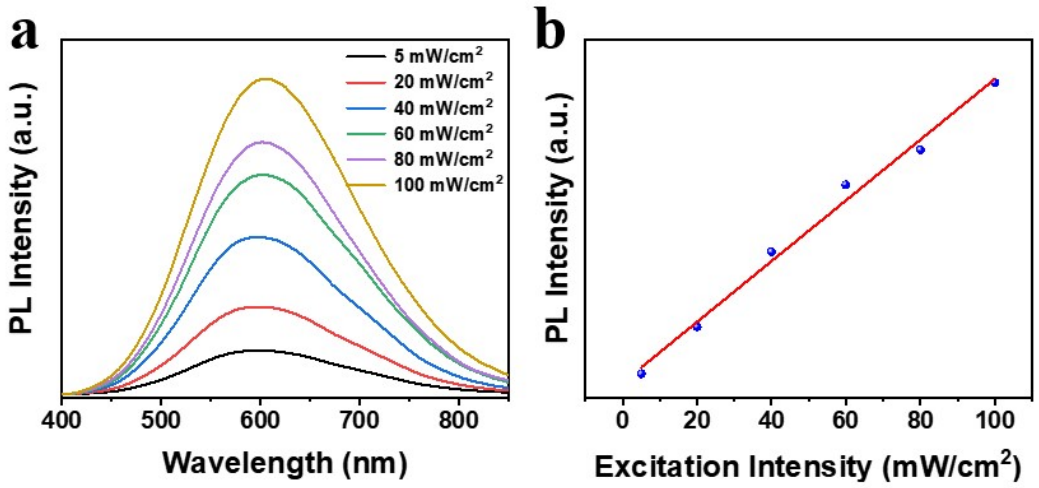

Figure S8. (a) Power dependence PL spectra for **1**. (b) The PL intensity versus excitation power of **1**.

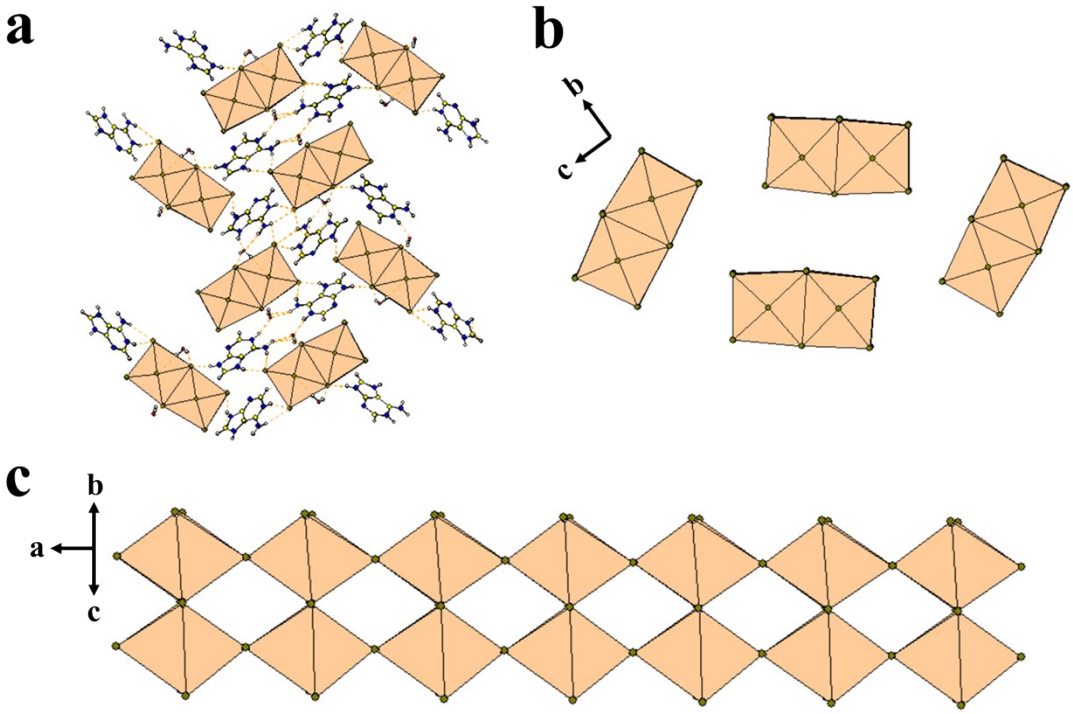

Figure S9. Detailed view of crystal structure **2**. (a,b) Top-down view of **2**. (c) Side view of **2**.

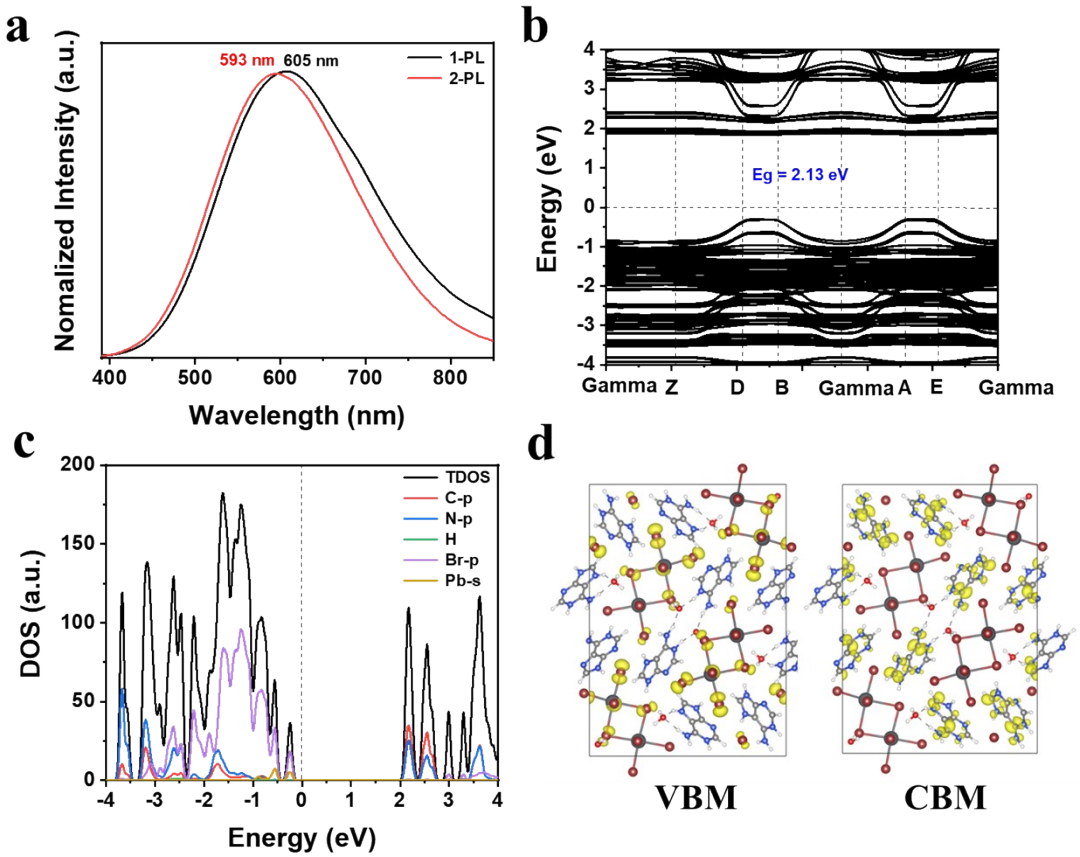

Figure S10. a) emission spectra) of **1** and **2**. b) DFT electronic band structure of **2**. c) Density of states of **2**. d) Spatial contour of antibonding (left) and bonding frontier orbitals (right) of **2**.

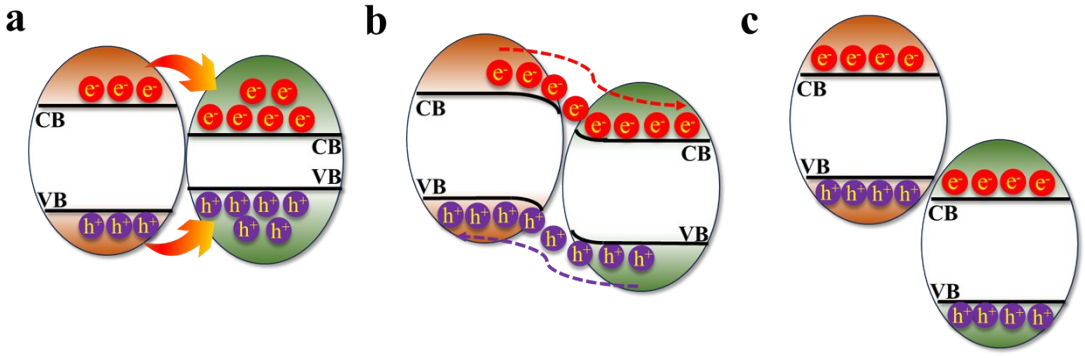

Figure S11. Schematic illustration of the three different types of heterojunction energy band arrangement: a) type-I, b) type-II, and c) type-III heterojunctions.

References

1. Kresse, G.; Furthmüller, J., Efficiency of ab-initio total energy calculations for metals and semiconductors using a plane-wave basis set. Comp. Mater. Sci. 1996, 6, 15.
2. Kresse, G.; Furthmüller, J., Efficient iterative schemes for ab initio total-energy calculations using a plane-wave basis set. Phys. Rev. B 1996, 54, 11169
3. Perdew, J. P.; Burke, K.; Ernzerhof, M., Generalized Gradient Approximation Made Simple. Phys. Rev. Lett. 1996, 77, 3865.
4. Kresse, G.; Joubert, D., From ultrasoft pseudopotentials to the projector augmented-wave method. Phys. Rev. B 1999, 59, 1758.
5. Blochl, P., Projector augmented-wave method. Phys. Rev. B 1994, 50, 24.
6. Grimme, S.; Antony, J.; Ehrlich, S.; Krieg, H., A consistent and accurate ab initio parametrization of density functional dispersion correction (DFT-D) for the 94 elements H-Pu. J. Chem. Phys. 2010, 132, 154104.
7. Grimme, S.; Ehrlich, S.; Goerigk, L., Effect of the damping function in dispersion corrected density functional theory. J. Comput. Chem. 2011, 32, 1456.
8. M.A.L. Marques, E.K.U. Gross, "Time-dependent density functional theory," Annu. Rev. Phys. Chem., 55, 427-455 (2004).